Single-crystal growth and superconductivity in RbNi$_2$Se$_2$

Hui Liu,[1] Xunwu Hu,[1] Hanjie Guo ●,[2] Xiao-Kun Teng,[3] Huanpeng Bu,[2] Zhihui Luo,[1] Lisi Li ●,[1] Zengjia Liu,[1]
Mengwu Huo,[1] Feixiang Liang ●,[1] Hualei Sun,[1] Bing Shen,[1] Pengcheng Dai ●,[3] Robert J. Birgeneau,[4,5]
Dao-Xin Yao ●,[1] Ming Yi,[3] and Meng Wang ●[1,*]

[1]*Center for Neutron Science and Technology, Guangdong Provincial Key Laboratory of Magnetoelectric Physics and Devices,
School of Physics, Sun Yat-Sen University, Guangzhou 510275, China*
[2]*Neutron Science Platform, Songshan Lake Materials Laboratory, Dongguan, Guangdong 523808, China*
[3]*Department of Physics and Astronomy, Rice University, Houston, Texas 77005, USA*
[4]*Department of Physics, University of California, Berkeley, California 94720, USA*
[5]*Materials Science Division, Lawrence Berkeley National Laboratory, Berkeley, California 94720, USA*

We report the synthesis and characterization of RbNi$_2$Se$_2$, an analog of the iron chalcogenide superconductor Rb$_x$Fe$_2$Se$_2$, via transport, angle-resolved photoemission spectroscopy, and density functional theory calculations. A superconducting transition at $T_c = 1.20$ K is identified. In the normal state, RbNi$_2$Se$_2$ shows paramagnetic and Fermi-liquid behaviors. A large Sommerfeld coefficient yields an effective electron mass of $m^* \approx 6m_e$. In the superconducting state, zero-field electronic specific-heat data C_{es} can be described by a two-gap BCS model, indicating that RbNi$_2$Se$_2$ is a possible multigap superconductor. Our density functional theory calculations and angle-resolved photoemission spectroscopy measurements demonstrate that RbNi$_2$Se$_2$ exhibits relatively weak correlations and multiband characteristics, consistent with the multigap superconductivity.

I. INTRODUCTION

Since the discovery of copper oxide superconductors, researchers have extensively searched for superconductivity in materials with transition metals [1,2]. Significant progress has been made in iron pnictide and chalcogenide compounds, where several structural systems have been identified with the highest T_c of 55 K achieved in LaFeAsO [3]. Superconductivity was also observed in the compounds containing Cr, Mn, and Eu under pressure, such as CrAs, KCrAs, CrSiTe$_3$, MnP, and EuTe$_2$ [4–8]. Among all of them, superconductivity has been found to be in the vicinity of an antiferromagnetic (AF) or ferromagnetic (FM) order. Nickel oxide materials have analogous structures with copper oxide superconductors. Superconductivity with $T_c = 9-15$ K has also been observed in films of nickel-based compounds [9–11].

ANi$_2$Se$_2$ (A = K, Cs, and Tl) crystalizes in the ThCr$_2$Si$_2$ structure and shows metallic behavior and Pauli paramagnetism. At low temperatures, superconductivity emerges with the superconducting (SC) transition temperatures of $T_c \approx 0.8$ K for KNi$_2$Se$_2$ polycrystals, 2.7 K for CsNi$_2$Se$_2$, and 3.7 K for TlNi$_2$Se$_2$ single crystals [12–14], while K$_{0.95}$Ni$_{1.86}$Se$_2$ single crystals do not show superconductivity down to 0.3 K, suggesting that the superconductivity is sensitive to the stoichiometry of the samples [15]. As a comparison, the A_xFe$_2$Se$_2$ system exhibits T_c ranging from 20 to 30 K. With a different amount of iron vacancies, A_xFe$_{2-\delta}$Se$_2$ exhibits a variety of AF orders and iron vacancy orders [16–19]. The replacement of Fe by Co suppresses the superconductivity and induces a FM order in RbCo$_2$Se$_2$ [20,21]. The ANi$_2$Se$_2$

superconductors with a formal valent state of Ni$^{1.5+}$ have been revealed to exhibit remarkable properties. In particular, they usually exhibit a large Sommerfeld coefficient γ, suggesting a large density of states and unconventional pairing at low temperature [13,14]. One possibility that was proposed was that the large Sommerfeld coefficient might be induced by local charge order [12]. However, angle-resolved photoemission spectroscopy (ARPES) measurements yield weak electronic correlations in KNi$_2$Se$_2$ and TlNi$_2$Se$_2$. The origin of the large Sommerfeld coefficient may be driven by the large density of states at the Fermi energy and the Van Hove singularity in the vicinity of the Fermi energy [22,23].

In this work, we report the successful synthesis and characterization of RbNi$_2$Se$_2$ single crystals. The crystal structure, electronic band structure, and transport properties have been investigated. We find that RbNi$_2$Se$_2$ is a Pauli paramagnetism and exhibits a SC transition at $T_c = 1.20$ K. Normal-state specific-heat measurements suggest an effective electronic mass enhancement with $m^* \approx 6m_e$. In the SC state, a two-gap BCS model can match well with the zero-field electronic specific heat, indicating that RbNi$_2$Se$_2$ is a possible multigap superconductor. Comparison with the density functional theory (DFT) calculations and ARPES measurements reveals that RbNi$_2$Se$_2$ is a weakly correlated superconductor with multibands crossing the Fermi level.

II. EXPERIMENTAL AND CALCULATION DETAILS

Single crystals of RbNi$_2$Se$_2$ were grown by the self-flux method [19,21]. The precursor NiSe was prepared by heating Ni powders and Se pellets at 500 °C. Then, the NiSe powders and Rb were put into an alumina crucible according
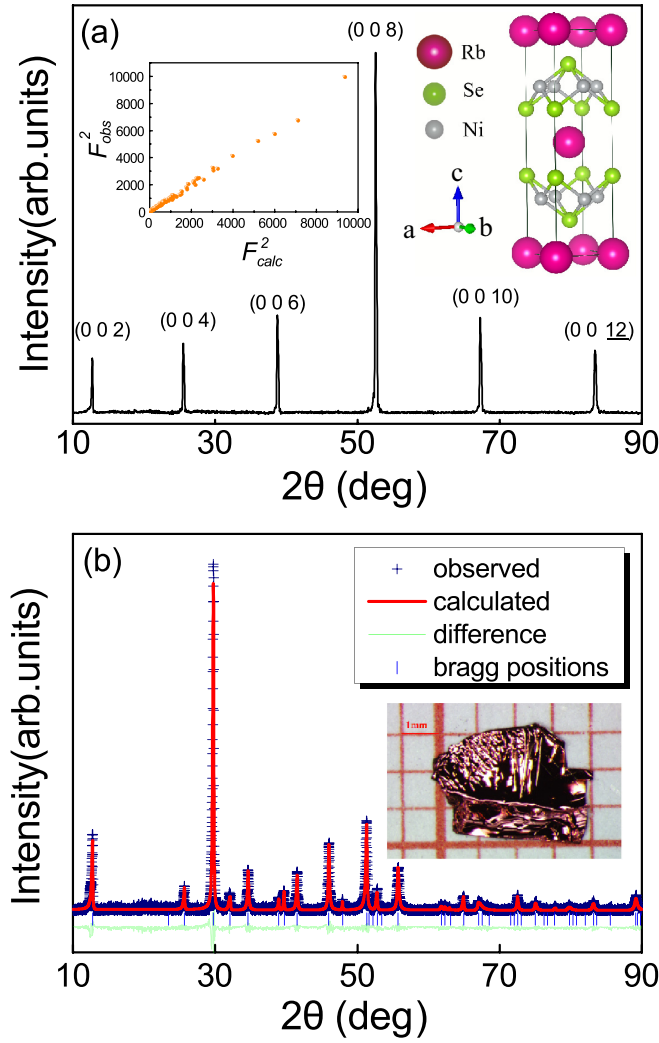
*wangmeng5@mail.sysu.edu.cn

FIG. 1. (a) XRD measurement on the *ab* plane of a RbNi$_2$Se$_2$ single crystal. The inset on the left is the refinement on single-crystal diffraction. The inset on the right shows the crystal structure. The pink, green, and gray balls represent Rb, Se, and Ni ions. (b) A pattern of XRD measured on powder samples. The inset is a photo of a RbNi$_2$Se$_2$ single crystal.

TABLE I. Single crystal of RbNi$_2$Se$_2$ refinement at 150 K.

Formula weight	223.14
Crystal system	Tetragonal
Space group	$I4/mmm$
Unit-cell parameters	$a = b = 3.9272(3)$ Å
	$c = 13.8650(5)$ Å
	$\alpha = \beta = \gamma = 90°$
Atomic parameters	
Rb	$2b(0, 0, 1/2)$
Ni	$4d(0, 1/2, 3/4)$
Se	$4e(1/2, 1/2, 0.6502(1))$
Density	3.466 g/cm^3
F(000)	198
Radiation	Mo $K\alpha$ ($\lambda = 0.7107$ Å)
2θ for data collection	$10.794°$ to $60.562°$
Index ranges	$-4 \leqslant h \leqslant 5, -5 \leqslant k \leqslant 5,$
	$-11 \leqslant l \leqslant 18$
Reflections collected	808
Independent reflections	119
Data/restraints/parameters	119/0/5
Goodness-of-fit on F^2	1.204
Final R indexes [$I \geqslant 2\sigma(I)$]	$R_1 = 0.0378, wR_2 = 0.1001$
Largest diff. peak/hole/e Å^{-3}	3.06/ -2.04

performed on a physical property measurement system with a dilution refrigerator (PPMS, Quantum Design). The in-plane resistivity $\rho_{ab}(T)$ was measured using the standard four-probe method on a rectangular sheet crystal to keep current flowing in the *ab* plane. The Vienna *Ab initio* Simulation Package (VASP) was employed for the DFT calculations [24]. ARPES measurements were performed on a helium-lamp-based system with a DA30 electron analyzer. Single crystals were cleaved *in situ* in ultrahigh vacuum with a base pressure better than 5×10^{-11} Torr at 30 K. Energy and angular resolutions were better than 20 meV and 0.1°, respectively.

III. RESULTS AND DISCUSSIONS

All peaks from single-crystal XRD can be indexed with the ThCr$_2$Si$_2$-type structure (space group $I4/mmm$), which are illustrated in the insets of Fig. 1(a). The determined lattice parameters are $a = b = 3.9272(3)$, and $c = 13.8650(5)$ Å at 150 K with the volume of the unit cell between that of KNi$_2$Se$_2$ and CsNi$_2$Se$_2$. Details of the atom coordinates and other key information are shown in Table I. To show the quality of the samples, we present a $\theta - 2\theta$ scan of a single crystal along the $(H = 0, K = 0, L)$ in Fig. 1(a) and an XRD pattern on a powder sample which was grounded from single crystals in Fig. 1(b), where (H, K, L) are Miller indices in reciprocal lattice units. No peaks from impurity could be identified. The EDS results for several single crystals are rather homogenous and the determined average atomic ratios are Rb:Ni:Se = 1.16(4):2.04(3):2.00 when the content of Se is normalized to be 2, close to the stoichiometry of RbNi$_2$Se$_2$.

The temperature dependence of the resistivity for RbNi$_2$Se$_2$ is shown in Fig. 2(a). The electric current is applied in the *ab* plane. The value of ρ_{ab} is about 92.1 $\mu\Omega$ cm at 300 K and only about 1.5 $\mu\Omega$ cm at 1.8 K. The residual resistivity ratio (RRR) of 61.4 [$\rho_{ab}(300$ K$)/\rho_{ab}(1.8$ K$)$] suggests

to stoichiometry and sealed in an evacuated silica tube. The mixture was kept at 150 °C for 5 h, then heated to 760 °C in 40 h and kept for 5 h; after that, it was heated to 1050 °C in 40 h and held for 5 h. The temperature was cooled down to 700 °C at a rate of 3.5 °C/h before the furnace was shut down. To prevent the reaction of Rb with water and air, all of the processes were conducted in an argon-filled glove box. Shiny platelike single crystals with a typical size of $4 \times 5 \times 1$ mm^3 were grown, as shown in the inset of Fig. 1(b). The samples are air sensitive and were kept in an argon-filled glove box. During the measurements, the samples were briefly exposed to air.

Single-crystal x-ray diffraction (XRD) was conducted on a SuperNova (Rigaku) x-ray diffractometer. The sample was blown by N$_2$ during the data collection to avoid exposure to air. The elemental analysis was measured using an energy-dispersive x-ray spectroscopy (EDS) (EVO, Zeiss). Electrical transport, magnetic, and specific-heat measurements were
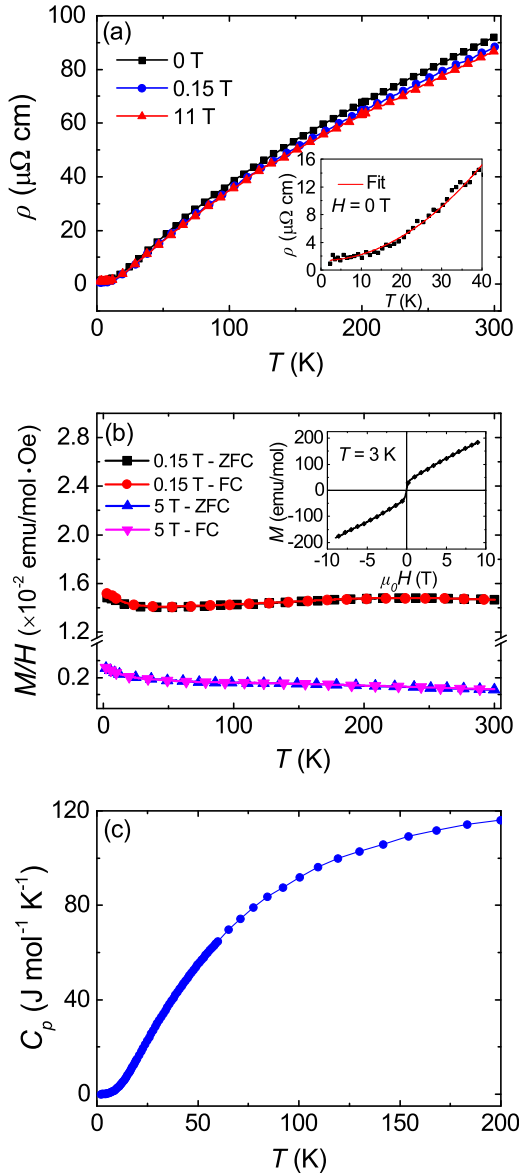
FIG. 2. (a) Temperature dependence of in-plane resistivity $\rho_{ab}(T)$ with magnetic fields $H = 0$, 0.15, and 11 T along the c axis. The inset shows the fitted result using $\rho_{ab}(T) = \rho_0 + AT^2$ from 1.8 to 40 K. The red line is a fitting curve. (b) Temperature dependence of ZFC and FC magnetic susceptibility with applying various external magnetic fields along the c axis. The inset shows a magnetization hysteresis loop at 3 K. (c) Temperature dependence of $C_p(T)$ from 2 to 300 K.

remarkable metallicity and high quality of the single crystals [15,25,26]. The resistivity measured at 0, 0.15, and 11 T shows a metallic behavior without any anomaly or obvious magnetic field dependence. The resistivity ρ_{ab} below 40 K can be well described by the equation $\rho_{ab}(T) = \rho_0 + AT^2$, as shown in the inset of Fig. 2(a), where $\rho_0 = 1.211\,\mu\Omega\,\text{cm}$ and $A = 0.012\,\mu\Omega\,\text{cm/K}^2$, consistent with a paramagnetic Fermi-liquid behavior [27]. The magnetic susceptibility is nearly independent of temperature, yielding a Pauli paramagnetic behavior as shown in Fig. 2(b). A weak FM sign is revealed from the hysteresis loop shown in the inset of Fig. 2(b), which could be ascribed to a small amount of Ni impurity [28]. The

contribution of Ni on the magnetization is estimated to be lower than 1%. The specific heat from 2 to 200 K shown in Fig. 2(c) also suggests that no phase transition occurs in this temperature range.

To explore the possible superconductivity, we show measurements down to 50 mK in Fig. 3. The magnetic susceptibility at low temperatures is shown in Fig. 3(a). A clear diamagnetic response appears below 1.20 K under zero field, indicating a SC transition. The transition shifts to lower temperatures with an increase of the dc bias field, consistent with the Meissner effect of superconductivity. With knowing $T_c \approx 0.8$ K for KNi$_2$Se$_2$ [12] and $T_c \approx 2.7$ K for CsNi$_2$Se$_2$ [13], the diamagnetic response at 1.20 K should correspond to the SC transition of RbNi$_2$Se$_2$. We plot the onset SC transition temperatures at various magnetic fields and fit the upper critical field $\mu_0 H_{c2}(0)$ using the Ginzburg-Landau theory with the formula $\mu_0 H_{c2}(T) = \mu_0 H_{c2}(0) \times (1 - t^2)/(1 + t^2)$, where t is the reduced temperature $t = T/T_c$. As shown in Fig. 3(b), the resultant $\mu_0 H_{c2}(0) = 1.38$ T is within the Pauli limit, $\mu_0 H_{c2}^p(0) = 2.37$ T, indicating a weak-coupling behavior [29].

Figure 3(c) displays the specific heat measured at low temperatures. In the normal state, a fit to the specific heat C_p from 1.5 to 3.8 K using $C_p/T = \gamma_N + \beta T^2$ results in the Sommerfeld coefficient $\gamma_N = 30.30\,\text{mJ}\,\text{mol}^{-1}\,\text{K}^{-2}$ and $\beta = 3.67\,\text{mJ}\,\text{mol}^{-1}\,\text{K}^{-4}$, as shown in the inset. The Debye temperature Θ_D is estimated to be 167 K from the equation $\Theta_D = (12\pi^4 NR/5\beta)^{1/3}$, where $N = 5$ is the number of atoms in each formula unit and R is the ideal gas constant. The γ_N for RbNi$_2$Se$_2$ is comparable with that of KNi$_2$Se$_2$ (~ 44 mJ mol^{-1} K^{-2}) [12], CsNi$_2$Se$_2$ (~ 77 mJ mol^{-1} K^{-2}) [13], and TlNi$_2$Se$_2$ (~ 40 mJ mol^{-1} K^{-2}) [14]. The effective mass of electrons m^* can be estimated through Eq. (1) [30],

$$m^* = \hbar^2 k_F^2 \gamma_N / \pi^2 n k_B^2, \qquad (1)$$

where k_B is the Boltzmann constant and the carrier density n is calculated by the number of electrons (Z) per cell volume (V). Using a spherical Fermi surface approximation, the Fermi wave vector can be estimated by $k_F = (3\pi^2 n)^{1/3}$. Assuming that Ni contributes 1.5 electrons ($Z = 6$), we obtain $k_F = 9.4 \times 10^9$ m^{-1}. The estimated effective mass of electrons $m^*/m_e = 6$ for RbNi$_2$Se$_2$ is significantly enhanced compared with the bare electron mass m_e. Combining the parameters from fitting the electronic specific heat and the quadratic temperature-dependent regime of resistivity, the Kadowaki-Woods ratio A/γ_N^2 is calculated to be $0.94 \times 10^{-5}\,\mu\Omega\,\text{cm}\,(\text{mol K}^2\,\text{mJ})^2$, close to $\sim 10^{-5}\,\mu\Omega\,\text{cm}\,(\text{mol K}^2\,\text{mJ})^2$ of heavy fermion systems [31]. This scaling relation indicates RbNi$_2$Se$_2$ exhibiting the heavy-fermion behavior.

In the SC state, the specific-heat data reveal an anomaly under zero field with a maximum at 0.85 K [Fig. 3(c)], suggesting bulk superconductivity. Applying an external magnetic field, the SC transition moves quickly to lower temperatures. As shown in the inset of Fig. 3(c), an upturn appears on C_p/T below $T^2 < 0.1$ K^2. The small upturn could be described by the Schottky anomaly for paramagnetic impurity spins [12], which can be well fitted by $C_N = D(H)T^{-2}$ with $D(H = 0) = 0.07$ mJ K mol^{-1}.

In order to get information about the SC gap, we extract the electronic specific heat C_{es} by subtracting the phonon
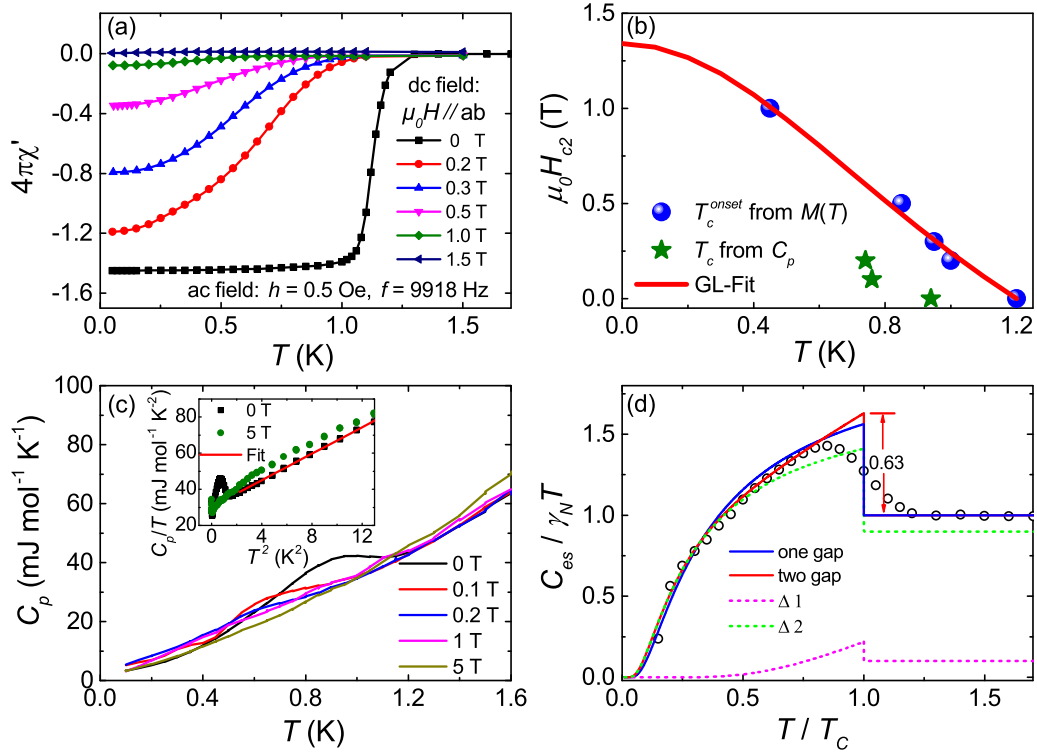
FIG. 3. (a) Diamagnetization of superconductivity under various magnetic fields. (b) Upper critical field H_{c2}, as a function of temperature. The blue circles and green stars are derived from the onset of magnetization and the specific heat based on an entropy-conserving construction. The red solid line shows a fit with the Ginzburg-Landau expression, as discussed in the text. (c) The low-temperature specific heat of RbNi$_2$Se$_2$, measured at various fields near the superconducting transition. The inset shows the Schottky anomaly at zero field and 5 T and a fitting of C_p in the normal state. (d) Reduced temperature T/T_c dependence of electronic specific heat divided by temperature and γ_N, $C_{es}/\gamma_N T$, in the SC state at zero field, where $C_{es} = C_p - C_{\text{lattice}} - C_N$. The two solid lines show the fitting curves of the one-gap BCS model and the two-gap model to $C_{es}/\gamma_N T$, respectively. The dashed lines show the contributions from two different gaps, Δ_1 and Δ_2, respectively.

contribution C_{lattice} that is extrapolated from the fitting in the normal state with zero field and Schottky anomaly C_N from the total C_p, $C_{es} = C_p - C_{\text{lattice}} - C_N$. The electronic specific-heat data $C_{es}(\gamma_N T)^{-1}$ against T/T_c are shown in Fig. 3(d), where γ_N has been revealed in the normal state. The T_c is determined to be 0.94 K using an equal-area entropy construction. The heat jump at the transition is 0.63, smaller than that of the theoretical value of 1.43 in the BCS weak-coupling scenario [32]. We employ both one-gap and two-gap BCS models $C_{es} = \sum C_i \exp(-\Delta_i/k_B T)$ to fit the electronic specific heat, where Δ_i is the size of the ith SC gap at 0 K. The one-gap model reveals $\Delta_0/k_B T_c = 0.30$ that is smaller than the value of 1.76 in the BCS theory [33]. In the two-gap model, the total specific heat can be considered as the sum of electronic contributions from two bands. Our fitting yields the sizes of two gaps of $\Delta_1/k_B T_c = 2.51$ and $\Delta_2/k_B T_c = 0.25$, respectively. The ratio of the contributions from the two gaps is $\sim 1.5 : 1$ as presented by the dashed lines in Fig. 3(d). The better fitting using the two-gap model indicates that RbNi$_2$Se$_2$ may be a multigap superconductor.

The electron-phonon coupling strength is also calculated by employing the inverted McMillan formula [34],

$$\lambda_{ep} = \frac{1.04 + \mu^* \ln(\Theta_D/1.45 T_c)}{(1 - 0.62\mu^*)\ln(\Theta_D/1.45 T_c) - 1.04}, \quad (2)$$

where μ^* represents the Coulomb repulsion pseudopotential, which we adopt as $\mu^* = 0.13$ for this system [35].

Generally, the λ_{ep} for strongly coupled superconductors are close to 1, and $\lambda_{ep} \rightarrow 0.5$ is viewed as weak-coupled superconductors [34]. The λ_{ep} for RbNi$_2$Se$_2$ is 0.49, suggesting that RbNi$_2$Se$_2$ is a weakly coupled superconductor, consistent with the specific-heat analysis.

To check the multiband character, we conducted DFT calculations and ARPES measurements on the electronic band structure. Figures 4(a) and 4(b) show the calculated electronic bands of Ni ions and the integrated density of states of Ni, Rb, and Se. The electronic states near the Fermi surface are governed by the 3d orbitals of Ni ions. In Fig. 4(c), the measured electronic structure of RbNi$_2$Se$_2$ is compared with the band structure obtained from the DFT calculations. The calculated curves (black lines) are scaled and overlaid onto the photoemission intensity along the $\Gamma - M$ direction. The theoretical and experimental data match qualitatively with a renormalization factor of about 1.8. This factor is relatively small compared to other iron-based superconductors [36], indicating that the electronic correlations are moderate. The moderate correlations suggest that the superconductivity is most likely originated from the electron-phonon coupling, similar to the two-gap superconductor MgB$_2$ [37,38]. Figure 4(d) shows the photoemission intensity map of the Fermi surface, overlaid with the DFT-calculated Fermi surfaces. The observed multiple Fermi pockets are consistent with the multiband behavior of this compound, reinforcing the condition for the two-gap feature in the SC state. The band structure is
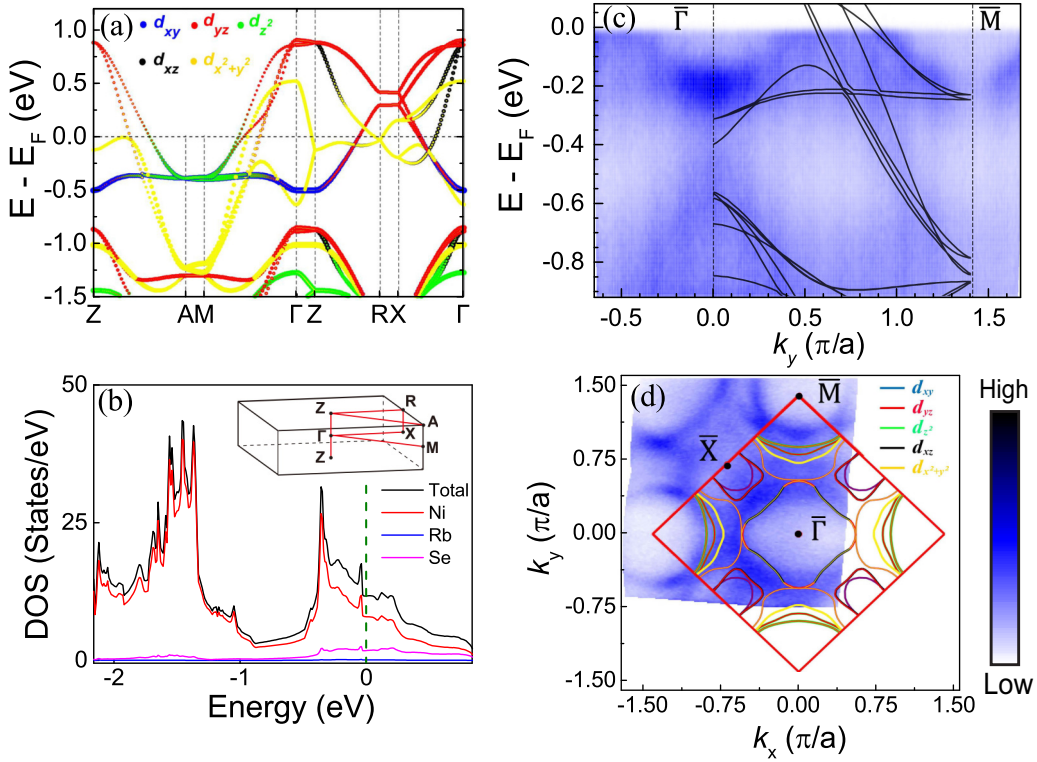
FIG. 4. (a) Projected band structure of Ni $3d$ in RbNi$_2$Se$_2$. Colors of the circle represent the different nickel orbitals, and the weight of each orbital is displayed by the size of the circles. The dashed lines are a guide to the eyes. (b) Density of states (DOS) near the Fermi level of RbNi$_2$Se$_2$. The red, blue, and purple curves represent contributions from Ni, Rb, and Se, respectively. Inset: The coordinates of the high-symmetry **k** path in reciprocal space of the tetragonal unit cell. (c) Measured spectral images along the high-symmetry direction $\Gamma \sim M$. The black lines are the band structure calculated by the DFT. (d) The Fermi surface mapping at 35 K, with the Brillouin zone (BZ) marked by a red square.

reminiscent of the closely related compound RbCo$_2$Se$_2$ [21]. However, the $3d_{x^2+y^2}$ flat band that induces itinerant ferromagnetism in RbCo$_2$Se$_2$ is observed here to be well below the Fermi level, due to the electron doping resulting from the replacement of Co by Ni. A progressive substitution of Ni by Co is expected to uplift the peak in DOS at $\sim$0.4 eV to the Fermi level.

As ANi$_2$Se$_2$ (A = K, Cs, and Tl) superconductors, RbNi$_2$Se$_2$ also exhibits an enhanced effective electron mass with a large Sommerfeld coefficient from specific heat. However, ARPES data reveal that the electronic correlation is not strong. To understand the reason for the large Sommerfeld coefficient, γ is estimated with λ_{ep} and $N(0)$ at the Fermi level through the relationship [39]

$$\gamma = \frac{\pi^2 k_B^2 N(E_F)(1 + \lambda_{ep})}{3}. \quad (3)$$

From the DOS in Fig. 4(b), $N(E_F)$ is estimated to be 11.68 states/eV per formula, resulting in $\gamma = 40.98$ mJ mol^{-1} K^{-2} that is close to the experimental value of 30.30 mJ mol^{-1} K^{-2}. Therefore, the result suggests that the large γ_N is related to the large DOS at the Fermi level as proposed in KNi$_2$Se$_2$ [22], instead of the heavy-fermion state. We note that the electron-paramagnon interactions will also play a role in this system, while an estimation of the effect on the Sommerfeld coefficient is beyond the scope of this work [40]. For ANi$_2$Se$_2$ (A = K, Rb, and Cs), the increase of the atomic radii of

the alkali metals works as applying a pressure to the Ni-Se layers. The DOS of Ni $3d$ orbitals at the Fermi surface, the Sommerfeld coefficient γ_N, and the electronic correlations are all enhanced. In the framework of the BCS theory, the SC transition temperature T_c increases accordingly, as the experimental observations in KNi$_2$Se$_2$, RbNi$_2$Se$_2$, and CsNi$_2$Se$_2$ [12–14].

IV. SUMMARY

In summary, we have successfully synthesized single crystals of RbNi$_2$Se$_2$ and characterized the physical properties. RbNi$_2$Se$_2$ is found to be a weakly coupled superconductor with T_c = 1.2 K. In the normal state, RbNi$_2$Se$_2$ exhibits the Fermi-liquid behavior and Pauli paramagnetism. In the SC state, the zero-field electronic specific heat can be well described with a two-gap BCS model, indicating that RbNi$_2$Se$_2$ possesses a multigap feature. DFT calculations and ARPES measurements demonstrate that multi-electronic bands of the $3d$ orbitals of Ni ions cross the Fermi level. Our analyses reveal that the large Sommerfeld coefficient of RbNi$_2$Se$_2$ is originated from the large DOS at the Fermi surface.

[1] J. G. Bednorz, M. Takashige, and K. A. Müller, Europhys. Lett. **3**, 379 (1987).

[2] K. Takada, H. Sakurai, E. Takayama-Muromachi, F. Izumi, R. A. Dilanian, and T. Sasaki, Nature (London) **422**, 53 (2003).

[3] Z.-A. Ren, G.-C. Che, X.-L. Dong, J. Yang, W. Lu, W. Yi, X.-L. Shen, Z.-C. Li, L.-L. Sun, F. Zhou *et al.*, Europhys. Lett. **83**, 17002 (2008).

[4] W. Wu, J. Cheng, K. Matsubayashi, P. Kong, F. Lin, C. Jin, N. Wang, Y. Uwatoko, and J. Luo, Nat. Commun. **5**, 5508 (2014).

[5] Q.-G. Mu, B.-B. Ruan, B.-J. Pan, T. Liu, J. Yu, K. Zhao, G.-F. Chen, and Z.-A. Ren, Phys. Rev. B **96**, 140504(R) (2017).

[6] J.-G. Cheng, K. Matsubayashi, W. Wu, J. P. Sun, F. K. Lin, J. L. Luo, and Y. Uwatoko, Phys. Rev. Lett. **114**, 117001 (2015).

[7] W. Cai, H. Sun, W. Xia, C. Wu, Y. Liu, H. Liu, Y. Gong, D.-X. Yao, Y. Guo, and M. Wang, Phys. Rev. B **102**, 144525 (2020).

[8] H. Sun, L. Qiu, Y. Han, Y. Zhang, W. Wang, C. Huang, N. Liu, M. Huo, L. Li, H. Liu *et al.*, arXiv:2206.06621.

[9] D. Li, K. Lee, B. Y. Wang, M. Osada, S. Crossley, H. R. Lee, Y. Cui, Y. Hikita, and H. Y. Hwang, Nature (London) **572**, 624 (2019).

[10] Q. Gu and H.-H. Wen, Innov. **3**, 100202 (2022).

[11] X. Ding, S. Shen, H. Leng, M. Xu, Y. Zhao, J. Zhao, X. Sui, X. Wu, H. Xiao, X. Zu *et al.*, Sci. China Phys. Mech. Astron. **65**, 267411 (2022).

[12] J. R. Neilson, A. Llobet, A. V. Stier, L. Wu, J. Wen, J. Tao, Y. Zhu, Z. B. Tesanovic, N. P. Armitage, and T. M. McQueen, Phys. Rev. B **86**, 054512 (2012).

[13] Huimin Chen, Jinhu Yang, Chao Cao, Lin Li, Qiping Su, Bin Chen, Hangdong Wang, Qianhui Mao, Binjie Xu, Jianhua Du, and Minghu Fang, Supercond. Sci. Technol. **29**, 045008 (2016).

[14] H. Wang, C. Dong, Q. Mao, R. Khan, X. Zhou, C. Li, B. Chen, J. Yang, Q. Su, and M. Fang, Phys. Rev. Lett. **111**, 207001 (2013).

[15] H. Lei, M. Abeykoon, K. Wang, E. S. Bozin, H. Ryu, D. Graf, J. B. Warren, and C. Petrovic, J. Phys.: Condens. Matter **26**, 015701 (2014).

[16] J. Guo, S. Jin, G. Wang, S. Wang, K. Zhu, T. Zhou, M. He, and X. Chen, Phys. Rev. B **82**, 180520(R) (2010).

[17] M. Fang, H. Wang, C. Dong, and Q. Huang, J. Phys.: Conf. Ser. **449**, 012015 (2013).

[18] P. Dai, Rev. Mod. Phys. **87**, 855 (2015).

[19] M. Wang, M. Yi, W. Tian, E. Bourret-Courchesne, and R. J. Birgeneau, Phys. Rev. B **93**, 075155 (2016).

[20] J. Yang, B. Chen, H. Wang, Q. Mao, M. Imai, K. Yoshimura, and M. Fang, Phys. Rev. B **88**, 064406 (2013).

[21] J. Huang, Z. Wang, H. Pang, H. Wu, H. Cao, S.-K. Mo, A. Rustagi, A. F. Kemper, M. Wang, M. Yi *et al.*, Phys. Rev. B **103**, 165105 (2021).

[22] Q. Fan, X. P. Shen, M. Y. Li, D. W. Shen, W. Li, X. M. Xie, Q. Q. Ge, Z. R. Ye, S. Y. Tan, X. H. Niu *et al.*, Phys. Rev. B **91**, 125113 (2015).

[23] N. Xu, C. E. Matt, P. Richard, A. van Roekeghem, S. Biermann, X. Shi, S.-F. Wu, H. W. Liu, D. Chen, T. Qian, N. C. Plumb, M. Radovic, H. Wang, Q. Mao, J. Du, M. Fang, J. Mesot, H. Ding, and M. Shi, Phys. Rev. B **92**, 081116(R) (2015).

[24] G. Kresse and J. Hafner, Phys. Rev. B **47**, 558 (1993).

[25] A. Ehrlich and D. Rivier, J. Phys. Chem. Solids **29**, 1293 (1968).

[26] A. E. Böhmer, V. Taufour, W. E. Straszheim, T. Wolf, and P. C. Canfield, Phys. Rev. B **94**, 024526 (2016).

[27] J. G. Analytis, H.-h. Kuo, R. D. McDonald, M. Wartenbe, P. M. C. Rourke, N. E. Hussey, and I. R. Fisher, Nat. Phys. **10**, 194 (2014).

[28] Q. Li, C. He, J. Si, X. Zhu, Y. Zhang, and H.-H. Wen, Commun. Mater. **1**, 16 (2020).

[29] J.-K. Bao, J.-Y. Liu, C.-W. Ma, Z.-H. Meng, Z.-T. Tang, Y.-L. Sun, H.-F. Zhai, H. Jiang, H. Bai, C.-M. Feng *et al.*, Phys. Rev. X **5**, 011013 (2015).

[30] L. E. DeLong, R. P. Guertin, S. Hasanain, and T. Fariss, Phys. Rev. B **31**, 7059 (1985).

[31] K. Kadowaki and S. Woods, Solid State Commun. **58**, 507 (1986).

[32] J. M. Daams and J. P. Carbotte, J. Low Temp. Phys. **43**, 263 (1981).

[33] J. Bardeen, L. N. Cooper, and J. R. Schrieffer, Phys. Rev. **108**, 1175 (1957).

[34] W. L. McMillan, Phys. Rev. **167**, 331 (1968).

[35] A. Amon, E. Svanidze, R. Cardoso-Gil, M. N. Wilson, H. Rosner, M. Bobnar, W. Schnelle, J. W. Lynn, R. Gumeniuk, C. Hennig *et al.*, Phys. Rev. B **97**, 014501 (2018).

[36] M. Yi, Y. Zhang, Z. Shen, and D. Lu, npj Quantum Mater. **2**, 57 (2017).

[37] F. Bouquet, Y. Wang, R. A. Fisher, D. G. Hinks, J. D. Jorgensen, A. Junod, and N. E. Phillips, Europhys. Lett. **56**, 856 (2001).

[38] F. Bouquet, R. A. Fisher, N. E. Phillips, D. G. Hinks, and J. D. Jorgensen, Phys. Rev. Lett. **87**, 047001 (2001).

[39] G. Xiao, Q. Zhu, Y. Cui, W. Yang, B. Li, S. Wu, G.-H. Cao, and Z. Ren, Sci. China Phys. Mech. Astron. **64**, 107411 (2021).

[40] P. K. G. Bedi, Physica C **596**, 1354049 (2022).